PAPER

Check for updates

Photoelectric effect of hybrid ultraviolet-sensitized phototransistors from an n-type organic semiconductor and an all-inorganic perovskite quantum dot photosensitizer†

Shao-Huan Hong, ‡[a] Shakil N. Afraj, ‡[b] Ping-Yu Huang, [b] Yi-Zi Yeh, [b] Shih-Huang Tung, [iD][c] Ming-Chou Chen [iD][b] and Cheng-Liang Liu [iD]*[d]

Low-dimensional all-inorganic perovskite quantum dots (QDs) have been increasingly developed as photo-sensing materials in the field of photodetectors because of their strong light-absorption capability and broad bandgap tunability. Here, solution-processed hybrid phototransistors built by a dithienothio-phenoquinoid (DTTQ) n-type organic semiconductor transport channel mixing with a colloidal $CsPbBr_3$ perovskite QD photosensitizer are demonstrated by manipulating the relative volume ratio from 10 : 0 to 9 : 1, 7 : 3, 5 : 5, 3 : 7, 1 : 9, and 0 : 10. This results in a significantly enhanced photodetection performance owing to the advantages of a high UV absorption cross-section based on the perovskite QDs, efficient carrier transport abilities from the DTTQ semiconductor, and the photogating effect between the bulk heterojunction photocarrier transfer interfaces. The optimized DTTQ : QD (3 : 7) hybrid phototransistor achieves a high photoresponsivity (R) of 7.1×10^5 A W^{-1}, a photosensitivity (S) of 1.8×10^4, and a photode-tectivity (D) of 3.6×10^{13} Jones at 365 nm. Such a solution-based fabrication process using a hybrid approach directly integrated into a sensitized phototransistor potentially holds promising photoelectric applications towards advanced light-stimulated photodetection.

1. Introduction

Photodetectors, which efficiently convert optical signals into electrical outputs, have been widely used in the various fields of photoactive optoelectronics, addressing a huge application spectrum including sensing, imaging, and communication.[1–17] Semiconductor-based photodetectors are generally categorized into three types, namely photodiodes, photoconductors, and phototransistors, depending on their device architecture and photoelectric mechanism.[1–4] Among these, lateral phototran-sistors with a metal–semiconductor-metal architecture forming a source/drain electrode and a gate electrode isolated by a dielectric layer are types of amplifying photoswitches, where the carrier density within a channel can be electrically

controlled by field-effect modulation and the incident light activates the channel conductance through the photogenerated carrier, which then profits by the photoresponse.[2,5] Current commercial photodetectors mainly use crystalline inorganic elemental materials, such as Si and III–V compound semi-conductors. The growth of these high-quality films *via* vapor deposition needs complicated manufacturing apparatus and large energy consumption. Therefore, vacuum-free and low-temperature solution-processed semiconductors are emerging as a class of photoactive materials for next-generation photodetection.

Low-dimensional perovskite materials have attracted increasing attention because of their unique photoelectric pro-perties and compatibility with various inorganic/organic components.[1,17,18] Therefore, semiconducting 0D perovskite quantum dots (QDs) with a superior extinction coefficient, large spectral coverage, and solution-processing ability are con-sidered to be ideal sensitizers for enhancing the photo-response. All-inorganic halide perovskite QDs exhibit improved stability among these perovskite-based materials, which make them potential candidates for photodetection applications. Because of the limited mobility of pristine perovskite materials, hybrid phototransistors fabricated by integrating an organic semiconductor transport layer with a light-absorbing

[a]*Department of Chemical and Materials Engineering, National Central University, Taoyuan 32001, Taiwan*
[b]*Department of Chemistry, National Central University, Taoyuan 32001, Taiwan*
[c]*Institute of Polymer Science and Engineering, National Taiwan University, Taipei 10617, Taiwan*
[d]*Department of Materials Science and Engineering, National Taiwan University, Taipei 10617, Taiwan. E-mail: liucl@ntu.edu.tw*
†Electronic supplementary information (ESI) available. See DOI: 10.1039/d1nr07084c
‡These authors contributed equally to this work.

perovskite QD layer provide the opportunity for photoelectrical performance improvement. Therefore, hybrid transistors give the low dark current because of the small intrinsic charge carrier concentration of organic semiconductors.[19] This results in high sensitivity and responsivity to the macroscopic photocurrent because of the photogating effect induced by the trapped carriers from the built-in potential at the heterointerface.[20–31] Some important photodetection parameters of hybrid transistors based on an organic semiconductor/perovskite QD heterojunction[32–35] reported in recent years have been listed in Table S1.† In early studies, Chen *et al.* fabricated bottom-gate dinaphtho[2,3-*b*:2′,3′-*f*]thieno[3,2-*b*]thiophene (DNTT) on which an additional layer of CsPbBr$_3$ perovskite QDs was deposited to form a double-layer heterojunction phototransistor.[35] DNTT improves the transportation of photoexcited charges, and consequently, the hybrid phototransistors exhibit the photoresponse performance in terms of a photoresponsivity (R) of 1.7×10^4 A W^{-1}, a photosensitivity (S) of 8.1×10^4, and a photodetectivity (D) of up to 2×10^{14} Jones. However, the top DNTT layer in this double-layer device was only deposited by thermal evaporation, which can not easily manipulate the relative composition in hybrids. Besides, both DNTT and CsPbBr$_3$ QDs have absorption peaks close to 460 nm, and thus, DNTT serves as both photosensitive and transport channel layers, which may be a compromise for light harvesting and charge transport.[35] In order to decouple the optical and electrical properties of the channel materials, a sensitized phototransistor can be introduced in this study, wherein the hybrid layer consists of organic semiconductors only favorable for the carrier transport between the channel and the perovskite layer for light absorption and photocarrier generation.[5,26,36,37] On the other hand, the vertical phase separation in this DNTT/QDs heterostructured bilayer results in limited exciton diffusion and charge separation, and thus hybrid bulk heterojunction nanostructures enable high exciton splitting efficiency by virtue of increasing the contact area in the photoactive layer, which has been widely used in previous photovoltaic-related devices.[38–42] Despite the hybrid concept in prototype building for phototransistors, there is a lack of knowledge about the morphological, microstructural, and photoelectric characteristics of the interfaces formed between the organic semiconductors and the all-inorganic perovskite QDs, particularly the direct blending of these two materials for the solution-processed bulk heterostructured photoactive layer in the hybrid sensitized phototransistor.

A UV photodetector that can convert UV light into electrical signals for monitoring has attracted substantial attention, as overexposure to UV light irradiation is a human health hazard that can lead to skin photoaging and ocular disease. CsPbBr$_3$ all-inorganic perovskite has a remarkable stability in air and strong absorption in the UV region.[43] In this paper, we report the simple solution-based fabrication and characterization of a hybrid UV-sensitized phototransistor on the basis of the bulk heterojunction of n-type dithienothiophenoquinoid (DTTQ)[44] small molecules and CsPbBr$_3$ all-inorganic perovskite QDs. The effects of QD loading in the hybrid and the UV light illu-

mination power were systematically investigated. Our comprehensive photoelectric characterization and microscopic study revealed that the microstructural morphologies and the molecular orientation within the hybrid films did not change obviously until the QD composition was up to 70% but exhibited an excellent photoresponse for UV light detection after sensitization with the CsPbBr$_3$ QD photoabsorber. The sensitization of DTTQ with CsPbBr$_3$ QDs in these hybrid films resulted in a photoresponsivity (R) as high as 7.1×10^5 A W^{-1}, a photosensitivity (S) of 1.8×10^4, and a photodetectivity (D) of 3.6×10^{13} Jones, which demonstrates one of the highest photoresponse parameters among QD-containing hybrid phototransistors (summarized in Table S1†). We interpreted the photoelectric phenomena as a result of the efficient photoexcited charge generation and charge transfer of free electrons from the QDs to DTTQ, and a mechanism related to the photodoping of the DTTQ channel by the photoexcited carriers of CsPbBr$_3$ QDs is proposed as well.

2. Experimental section

2.1. CsPbBr$_3$ QD preparation

The synthesis procedure was modified following the previously reported method. A CsPbBr$_3$ QD precursor solution was prepared by dissolving reagents of PbBr$_2$ and CsBr (1 : 1; 0.4 mmol) with a mixture of 60 μL of *n*-octylamine (OAm) and 2 mL of oleic acid (OA) in a solvent of DMF (10 mL) inside a N$_2$ glove box with stirring overnight at a temperature of 70 °C. The precursor was filtered with a 0.45-μm PVDF filter and then sprayed into 50 mL of toluene to form a yellow crude reaction dispersion. This dispersion was centrifuged for 10 min at 8000 rpm. The precipitated QDs were collected and redispersed in 8 mL of chlorobenzene. Finally, the resultant dispersion was centrifuged again at 6000 rpm for 10 min, and the supernatant (nanocrystal dispersion) was collected (~1.07 mg mL^{-1} in chlorobenzene) before use.

2.2. Device fabrication and measurement

Prior to phototransistor fabrication, a highly n-doped Si wafer and a SiO$_2$ (300 nm-thick) dielectric were rinsed by sonication in acetone and isopropanol for 5 min, respectively. The cleaned substrates were exposed to oxygen plasma for 5 min and then treated with a self-assembled monolayer of PETS in the solution phase (~1 μL mL^{-1} in toluene). The DTTQ organic semiconductor was dissolved in chlorobenzene at a concentration of 2 mg mL^{-1}. Then, the hybrid solution was obtained by mixing the prepared DTTQ and CsPbBr$_3$ QD solution at room temperature overnight with constant stirring according to the volume ratios of 9 : 1, 7 : 3, 5 : 5, 3 : 7, and 1 : 9 (respective weight ratios of 94%, 81%, 65%, 44%, and 17% of DTTQ in blend). The DTTQ : QD hybrid layers were formed by using the solution-shearing method at a shearing rate of 10–40 μm s^{-1} onto the preheated substrates (50–55 °C), followed by heating at 70 °C for 2 h under vacuum to form the crystalline phase. Finally, 80 nm-thick Ag layers were deposited by thermal evap-

oration under a base vacuum pressure of 4×10^{-6} torr at a deposition rate of ∼ 0.5 Å s^{-1}, and the source and drain electrodes were defined by the shadow mask. In the inverted staggered bottom-gate top-contact (BGTC) OFET structures, the channel length and width of the OFETs were 25 and 1500 μm, respectively. A Keithley 4200 semiconductor parameter analyzer connected to a customized probe station was used for the electrical measurement. For the measurements of the phototransistor performance, the channel area of the devices was illuminated with LEDs (center wavelength = 365 nm). The intensity of the LED light was controlled using a Keithley 2400 source meter, and the light intensity was calibrated using an analog optical power meter (Newport 1918-R). The fabricated phototransistors were stored inside a N$_2$-filled glove box before and after the measurements to protect them from moisture and oxygen.

3. Results and discussion

As schematically illustrated in Fig. S1,† colloidal CsPbBr$_3$ QDs were synthesized by the spray-assisted ligand-assisted re-precipitation (LARP) method,[45,46] which can control the size of QDs more efficiently than the conventional LARP with a dropping process. Inorganic salts and surfactants (oleic acid and octylamine) were dispersed in a polar DMF solvent, and then, this precursor mixture was sprayed into the nonpolar toluene solvent, which triggered the nucleation and growth of the perovskite QDs under the supersaturated recrystallization conditions. The purification of the perovskite QD solution could be obtained by the following centrifugation process and then storing the received particles in chlorobenzene. According to the morphological features revealed by transmission electron microscopy (TEM; Fig. S2(a)†), the CsPbBr$_3$ QDs presented a nearly cubic shape with a uniform size of ∼5 nm. The phase structure of the as-synthesized CsPbBr$_3$ nanocrystals was further characterized by high-resolution TEM (HRTEM), selected area electron diffraction (SAED) patterns, and X-ray diffraction (XRD) patterns. The HRTEM image in Fig. 1(a) reveals the highly crystalline nature of CsPbBr$_3$ QDs and the lattice fringe pattern with an interplanar lattice spacing of 0.41 nm corresponding to the (110) planes.[35] In addition, the reciprocal lattice points from three intense diffraction rings of the CsPbBr$_3$ nanocrystals on the Cu grid were verified in the SAED pattern shown in Fig. S2(b).† In Fig. 1(b), the XRD spectrum of the CsPbBr$_3$ film shows six splitting reflection peaks at $2\theta = 15.3°, 21.5°, 30.7°, 34.5°, 37.4°,$ and 43.7° assigned to the (100), (110), (200), (210), (211), and (220) planes of the perovskite phase,[35] respectively, representing cubic crystal structures with high crystallinity. The elemental composition analysis of CsPbBr$_3$ QDs was carried out by X-ray photoelectron spectroscopy (XPS), as shown in Fig. S3.† The high-resolution spectra of Cs 3d, Pb 4f, and Br 3d were surveyed next. The Cs 3d spectrum (Fig. S3(a)†) also showed doublets at around 740.3 and 726.2 eV, assigned to 3d$_{3/2}$ and 3d$_{5/2}$, respectively. The Pb 4f spectrum (Fig. S3(b)†) for QD films was recorded for
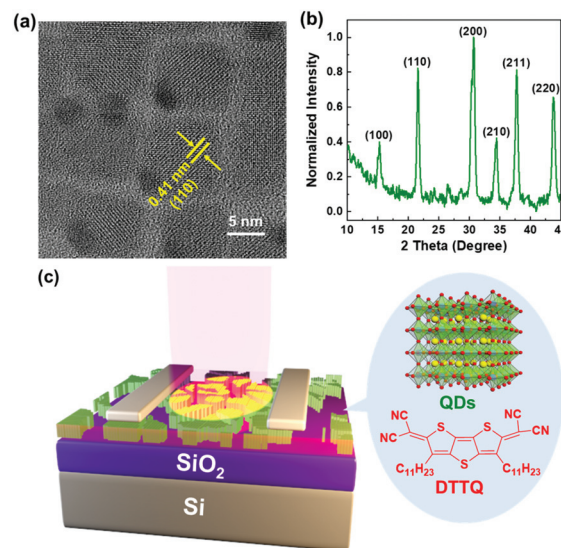

Fig. 1 (a) HR-TEM image and (b) XRD spectrum of CsPbBr$_3$ QDs. (c) Schematic illustration of the hybrid DTTQ:QD sensitizer phototransistor.

two contributions 4f$_{5/2}$ and 4f$_{7/2}$ located at the binding energies of 143.3 and 138.3 eV, respectively, corresponding to the Pb^{2+} cation. Moreover, Br 3d could be fitted into two sub-peaks at the binding states of 69.8 and 68.9 eV (Fig. S3(c)†). The surface elemental composition revealed a Cs:Pb:Br atomic ratio of 0.99:1.00:2.94, which was close to the theoretical value of 1:1:3. This might help the inhibition of surface traps in CsPbBr$_3$ QDs prepared by a spraying-assisted process.[47,48]

For the preparation of the DTTQ:QD hybrid blend solutions, the individual DTTQ and QD colloidal solutions were mixed in the controlled ratios of 10:0, 9:1, 7:3, 5:5, 3:7, 1:9, and 0:10, respectively. Note that the hybrid suspension remained stable without any noticeable precipitation. Subsequently, in a one-step solution-sheared process, DTTQ:QD ($X:Y$) hybrid films (where $X + Y = 10$) were deposited onto the 2-(phenylethyl)trichlorosilane (PETS)-modified Si/SiO$_2$ substrates, followed by thermal annealing. Fig. 2 shows the surface morphology evaluation of DTTQ films on the PETS-modified Si/SiO$_2$ substrates after the introduction of CsPbBr$_3$ QDs obtained from the optical microscope (OM; Fig. 2(a)–(g)), the polarized optical microscope (POM; Fig. 2(h)–(n)), and the atomic force microscope (AFM; Fig. 2(o)–(u)). As shown in Fig. 2(g) and (n), the solution-sheared films of pristine CsPbBr$_3$ QDs without the DTTQ organic semiconductors showed widespread island-like grains of a brown-yellow color with a dimension of 5 μm, which resulted from the clustering of QDs. A poor coverage of the discrete QD agglomeration was detected on the substrate surface. In contrast, the micro-ribbon-shaped DTTQ crystals along the shearing direction were observed in the POM images (Fig. 2(h)), which possessed the same morphologies as those reported in our previous paper.[44] The OM/POM images shown in Fig. 2(b)–(f)/2(i)–(l) showed the results of adding CsPbBr$_3$
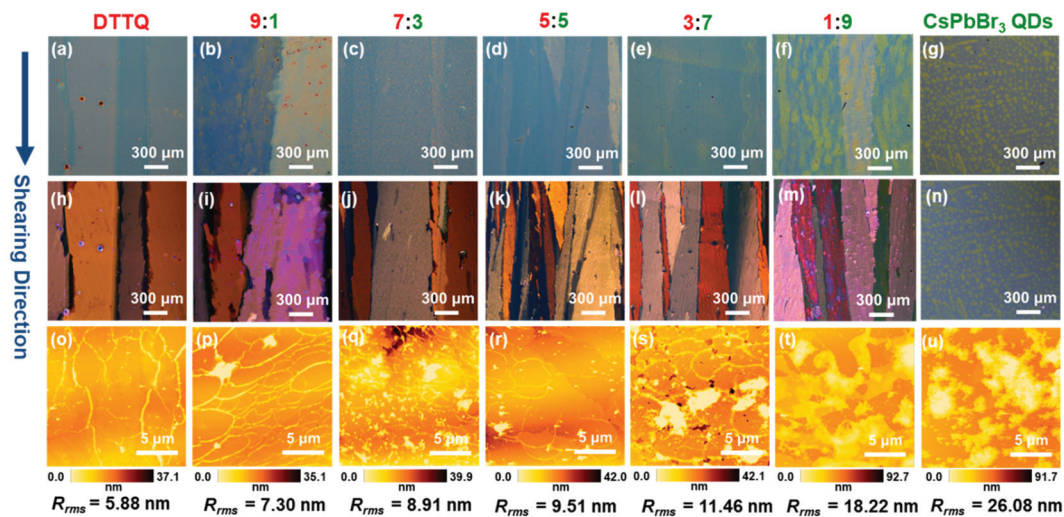
Fig. 2 (a–g) OM, (h–n) POM, and (o–u) AFM images of solution-sheared pristine DTTQ, CsPbBr$_3$ QDs, and hybrid DTTQ : QD films.

QDs to DTTQ small molecules. From the POM images, we inferred that the contrast of QDs inside the hybrid samples was considerably weaker than that of the DTTQ main body and thus was difficult to distinguish. However, it could be clearly seen in the OM images that the QDs lined up with the DTTQ crystals in the hybrid films. Upon the change in the hybrid composition ratio from 9 : 1 to 1 : 9, an increase in QDs indicated a larger QD domain gradually embedded in the DTTQ crystals. However, the island-like QDs aggregate in a larger scale for the DTTQ : QD (1 : 9) film. Note that the QD crystals were still distributed along the shearing direction during the hybrid film formation process. In particular, the pristine QD films only exhibit the dot-like features. Further investigation by topographic AFM also indicated the same morphological transition with the increased domain in the QD parts in the hybrids upon an increase in the QD loading, revealing that the QDs formed a physical contact with the organic crystals. Because of the different surface morphologies between the DTTQ and QDs, an increase in the aggregation and the surface roughness was observed in the hybrid films with respect to the pristine DTTQ. Obvious phase separation on a larger scale can be found in the DTTQ : QD (1 : 9) film with a highest root-mean-square (RMS) roughness (R_{rms}) of 18.22 nm in all hybrids. The phase image of the DTTQ : QD (3 : 7) film (Fig. S4†) clearly revealed the square-like QDs, which was close to the average size of QDs observed from the HRTEM images (Fig. 1(a)).

The distribution of QDs in the prepared hybrid layer was measured with a time-of-flight secondary ion mass spectrometer (TOF-SIMS). The TOF-SIMS detected the signals for Br$^-$, PbBr$^-$, S$^-$, CN$^-$, and Si$^-$ while sputtering through the film using an ion beam. The Br$^-$/PbBr$^-$ signal represents the vertical direction of the films with different amounts of QDs, while S$^-$/CN$^-$ is the fragment element associated with DTTQ. In Fig. S5,† we show the TOF-SIMS spectra of heterostructured hybrid films containing various compositions of QDs and

DTTQs deposited on the SiO$_2$/Si substrate. For all the hybrid films, the Si$^-$ signals increased with an increase in the depth in the films and then reached plateau values at the film/substrate interfaces. The Br$^-$, PbBr$^-$, S$^-$, and CN$^-$ signals did not significantly change with a change in depth before the Si$^-$ signals reached the plateau, indicating that the DTTQ : CsPbBr$_3$ QD bulk heterojunction existed inside the mixing layer deposited onto the Si/SiO$_2$ substrate and they were uniformly distributed across the entire films. Besides, the polygon-shaped QDs, especially for triangle-like, in the phase diagram of AFM images (Fig. S4†) were also proved to be well embedded in between the molecular layers of DTTQ.

To probe the influence of the CsPbBr$_3$ QDs on the DTTQ orientation with respect to the substrate, synchrotron two-dimensional (2D) grazing incidence X-ray diffraction (GIXRD) was further used to study the crystallography of the hybrid films with various compositions. Fig. 3 and S6† show the GIXRD profiles of neat DTTQ and CsPbBr$_3$ QDs as well as DTTQ : QDs hybrid films with various QD loading compositions. The resulting diffractograms for the DTTQ film (Fig. 3(a)) exhibited a series of diffraction profiles with spotty patterns, which demonstrated that highly textured DTTQ crystalline domains grew on the substrates, in agreement with our previous report.[44] In contrast, the pristine CsPbBr$_3$ QD film (Fig. 3(c)) exhibited a ring-like diffraction pattern, indicating a considerable randomness in the crystallite orientation. We observed that the diffraction rings at q = 1.11, 1.57, 2.22, 2.45, and 2.68 Å were assigned to the (100), (110), (200), (210), and (211) diffractions of the cubic perovskite phase with high crystallinity, which was in line with the 1D XRD pattern. All the hybrid films exhibited the combinations of the diffraction signals from the pure DTTQ and CsPbBr$_3$ QDs (Fig. 3(b) and S6†), which were indicative of the presence of the separated DTTQ and CsPbBr$_3$ QD phase in the films. Thus, we concluded that the preferred orientation of DTTQ and the crystal lattice
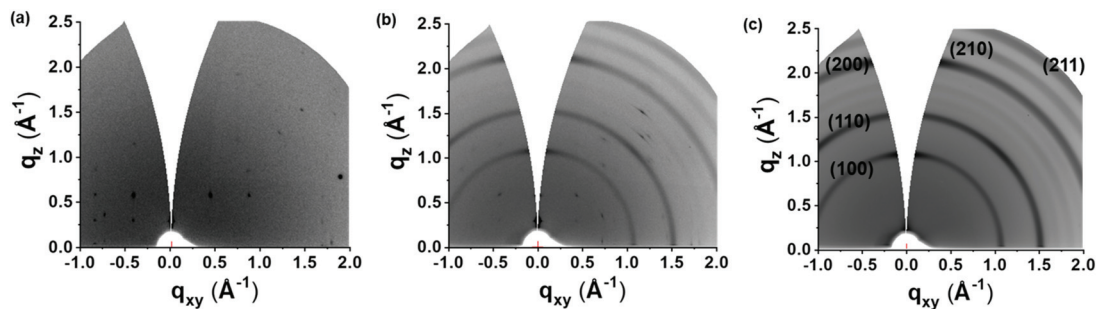
Fig. 3 2D GIXRD profiles of solution-sheared (a) DTTQ, (b) DTTQ : QD (3 : 7), and (c) CsPbBr$_3$ QD films.

of the CsPbBr$_3$ QDs remained unchanged after the mixing of these two components.

To investigate the optical characteristics of the DTTQ : CsPbBr$_3$ QD hybrid film, we performed the UV-Vis absorption and photoluminescence (PL) spectral analysis on the pristine DTTQ, CsPbBr$_3$, and their hybrid system. The absorption spectrum (Fig. 4(a)) of the pristine DTTQ layer presented two absorption peaks between 400 nm and 700 nm, whereas the CsPbBr$_3$ QDs exhibited a strong absorption below the 400 nm wavelength. In addition, the optical bandgap of CsPbBr$_3$ QDs was determined using the Tauc plot (Fig. S7†) from the absorption edge. The obtained direct bandgap for QDs was found to be 2.32 eV. The optical absorbance of the DTTQ : CsPbBr$_3$ QD (3 : 7) hybrid film was enhanced and broad below the 680 nm wavelength, which resulted from the synergetic absorption effect of the DTTQ : CsPbBr$_3$ QD blends. The improved absorption in the hybrid film which comes from the compatibility between DTTQ and QDs could potentially increase the phototransistor performance. Fig. 4(b) shows the PL properties of pristine and hybrid films on glass substrates. The PL spectra excited using a 405 nm laser were recorded, in which an evidence peak at 521 nm with a narrow FWHM of 28 nm was identified for pristine CsPbBr$_3$ QDs. However, it has been found that the pristine DTTQ film showed no or weak fluorescence emission over the 405 nm excitation wavelength. We also observed that the PL emission intensity of the DTTQ : QD (3 : 7)

hybrid film was quenched by ~54% after blending with DTTQ, which was mainly due to the efficient photoinduced charge transfer and exciton dissociation at the interfaces.[49,50]

The valence band edge (E_v) or HOMO energy level values of CsPbBr$_3$ QDs and DTTQ and their hybrids were characterized by photoelectron spectroscopy in air (PESA; Fig. S8†), and the conduction band edge (E_c) or LUMO energies were further determined according to their optical bandgap. Evidently, we found that E_v = −5.60 eV and HOMO = −5.90 eV for QDs and DTTQ, corresponding to the E_c = −3.28 eV and LUMO = −3.95 eV, respectively. Moreover, all the E_v values in the hybrids (−5.78~−5.62 eV for the DTTQ : QDs of 9 : 1 to 1 : 9) lay between the E_v value of QDs and the HOMO value of DTTQ, and then, the E_v value shifted towards a relatively shallow level when the QD loading was increased.

Next, the optical-electrical properties of the hybrid phototransistor with DTTQ : QD bulk heterojunction structures were investigated to make use of the driving force to separate the excited hole–electron pairs. The hybrid phototransistor architecture was fabricated with the device configuration shown in Fig. 1(c). For a bottom-gate top-contact (BGTC), a highly n-doped Si wafer with a 300 nm-thick SiO$_2$ layer was used as the gate electrode. The PETS layer was a surface modifier used to reduce the surface charge traps on SiO$_2$. The bulk heterojunction layer acted as a bridge to connect the CsPbBr$_3$ QD photo-absorbing components and the DTTQ semiconducting channel in the hybrid sensitized phototransistor. The Ag source and drain electrodes were thermally evaporated through a shadow mask to complete the hybrid phototransistor device. Fig. 5 show a comparison of the transfer (drain current–gate current (I_d–V_g)) characteristics of the CsPbBr$_3$ perovskite QD heterointerfaces with the semiconducting DTTQ materials in the dark and under the illumination of 365 nm UV light with different densities. In the dark, the pristine DTTQ device exhibited the gate voltage (V_g)-modulated current with a calculated mobility of ~0.2 cm^2 V^{-1} s^{-1} and an ON/OFF ratio greater than 10^5, whereas the DTTQ : CsPbBr$_3$ hybrid ones showed a slightly lower I_d value, possibly because of the reduced charge transport phases within the hybrids. Therefore, the dark I_d (I_{dark}) value at both ON and OFF states decreases as the loading amount of CsPbBr$_3$ QDs increases, which can be evidenced by the obvious QD aggregation phase
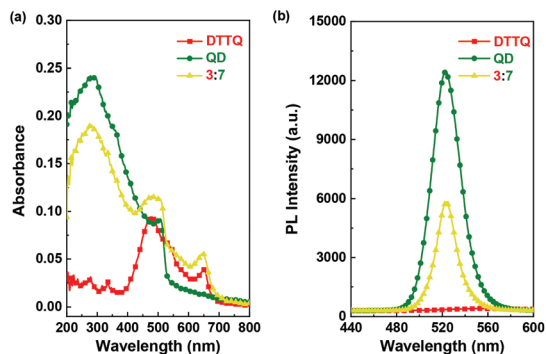

Fig. 4 (a) Absorption and (b) steady-state PL spectra of solution-sheared DTTQ, DTTQ : QD (3 : 7), and CsPbBr$_3$ QD films.
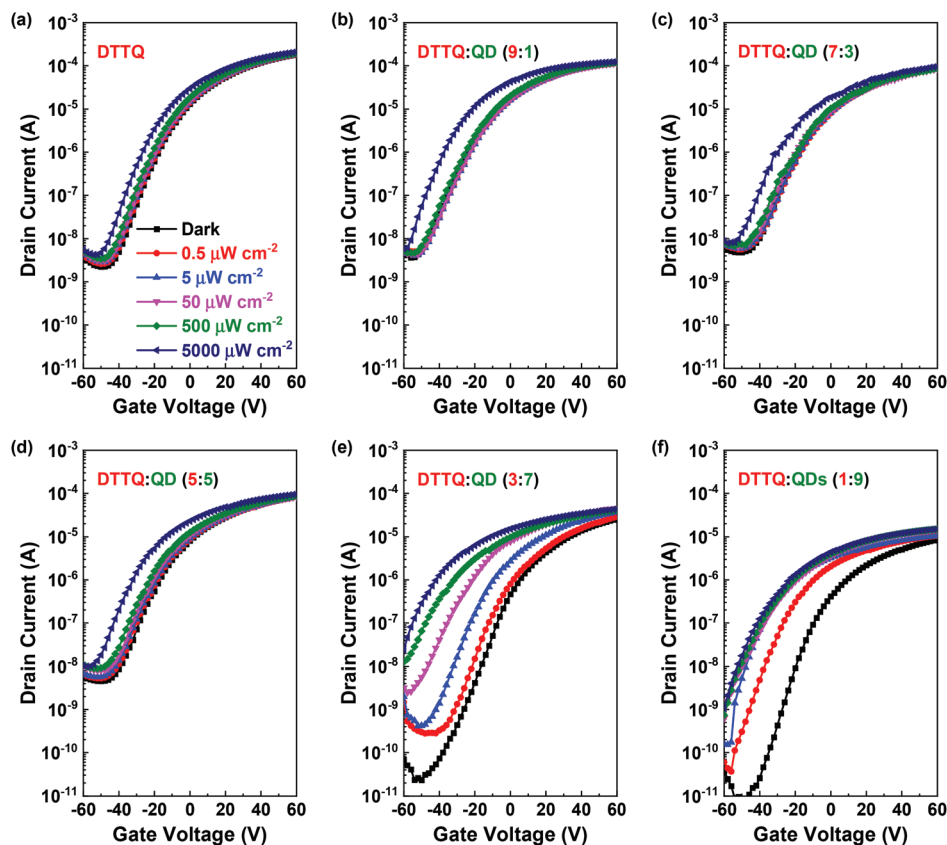
Fig. 5 Transfer characteristics of (a) DTTQ and hybrid DTTQ : QDs (b) (9 : 1), (c) (7 : 3), (d) (5 : 5), (e) (3 : 7) and (f) (1 : 9) phototransistors in the dark and under different excitations at 365 nm.

with an enhanced surface roughness. By varying the illumination intensities (from 0.5 to 5, 50, 500, and 5000 $\mu W\ cm^{-2}$) with V_g sweeping from −60 to 60 V at V_d = 60 V, we observed that the photo-induced I_d (I_{illum}) values of all the hybrid transistors considerably increased at a specific V_g value of −40 V more than that of the pristine DTTQ reference device before sensitization with QDs, indicating that the incorporation of the QDs effectively enhanced the device photoresponse. Meanwhile, the threshold voltage (V_{th}) was negatively shifted with increasing the effective incident light intensity (P_{eff}) in these hybrid phototransistors, as shown in the linearly-fitted curve between the threshold voltage shift (ΔV_{th}) and P_{eff} (Fig. S9†) for the DTTQ : QD (3 : 7) device, mainly due to the photoconductive effect dominated.[51–53] The output (drain current–drain current (I_d–V_d) characteristics of the DTTQ : QD (3 : 7) device in the dark and under illumination (5000 $\mu W\ cm^{-2}$) are also shown in Fig. S10.† The increase in the I_{illum} value (Fig. S10(b)†) compared with the I_{dark} value (Fig. S10(a)†) as a result of the photogeneration of excitons contributed to the non-saturation behavior in the output curve which was more remarkable for more positive V_g.

The pristine DTTQ device did not have an obvious response to a 365 nm LED because the energy of the 365 nm LED was above the bandgap of DTTQ, and thus the photocurrent generation took place exclusively in the QD layer. On the other hand, no field-effect current can be observed for the QD-only device (Fig. S11†), probably due to the poor disconnected dot-like aggregates with insulating surface-passivated ligands. The ΔV_{th} value between the dark and illumination (5000 $\mu W\ cm^{-2}$) is much more pronounced from 13.34, to 14.87, 16.00, and 50.05 V for the DTTQ : QD (9 : 1), (7 : 3), (5 : 5), and (3 : 7) devices, respectively, but decreases (29.21 V) for the highest QD loading in the DTTQ : QD (1 : 9) hybrid device (Fig. S12†). Here, a mechanism of the photocurrent behavior is described through the schematics of the energy band diagram combining with the spectroscopic analysis, as shown in Fig. 6. The band edges of the DTTQ : QD heterojunction were well aligned to form the staggered gap (type II, Fig. 6(a)). A clear offset in the electron affinities between DTTQ and the QDs accelerated the excited electrons in the conduction band of the QDs extracted to DTTQ, while the holes still accumulated in the perovskite QD layer because of the existing hole barrier at the interfaces.[21,54] We expected the electrons to only move along the lateral direction and accumulate in the DTTQ n-channel of the heterojunction between the sources and the drain in the dark state. Under UV light illumination, the hole–electron pairs were primarily generated in the light-absorbing $CsPbBr_3$ QD part of the hybrid layer, and parts of the photogenerated electrons were transferred into the DTTQ channel (Fig. 6(b)) because of the built-in potential which can be confirmed by
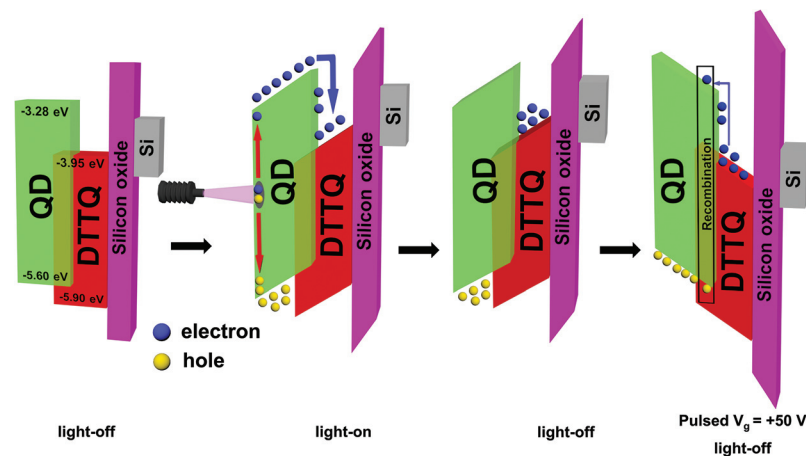
Fig. 6 Schematic representation of the operation mechanism of the hybrid phototransistor, including the energy-level diagram of the DTTQ : QD hybrid heterojunction and the light-stimulated charge transfer process from the CsPbBr$_3$ QDs to DTTQ.

the absorption and fluorescence spectra (Fig. 4), whereas the photogenerated holes were confined within the CsPbBr$_3$ QDs because of the high valence band barrier. This charge separation strongly suppressed the recombination in QDs,[55] and the light-stimulated charge transport process was in favor of enabling the DTTQ : CsPbBr$_3$ QD hybrid devices for light detection. Based on the analysis above, it can be concluded that the relatively high electron mobility of DTTQ can be introduced in the hybrid matrix to facilitate the charge transport and CsPbBr$_3$ QDs absorb the photons. Such a DTTQ : CsPbBr$_3$ QD hybrid phototransistor can offer the synergetic effect and possess both benefits from these two materials. As a result, the photogenerated excitons in the hybrid devices accompany the increase in QD loading of hybrids, as well as the illumination intensity. Among these, the DTTQ : QD (3 : 7) device showed the most significant enhancement in photo-induced I_d (at a V_g value of −40 V) and negatively-shifted V_{th} under light illumination (Fig. 5(e)), which could be attributed to the strong absorption in the QDs, efficient dissociation/separation of the photoexcited carriers, and an increase in the charge transport. However, further increase in the amounts of QDs (*e.g.* DTTQ : QD (1 : 9)) degraded the device photoresponse especially in ΔV_{th}, which is mainly attributed to the phase separated hybrid film morphology for significant aggregated QD domains. The charge transport in the DTTQ : QD (1 : 9) device is also lowered, originating from partial disruption in the molecular packing of DTTQ crystals. The curve of the logarithmic-plotted photocurrent ($I_{ph} = I_{illum} − I_{dark}$) as a function of P_{eff} is plotted, as shown in Fig. 7(a). Therefore, the photocurrent of this hybrid channel device increased sublinearly with an increase in the incident illumination power ($I_{ph} \sim P_{eff}^\alpha$). The calculated exponent (α) *via* linearly fitting the curve was 0.95, which implied the increased recombination activity of photogenerated charge carriers at an elevated light intensity due to the higher carrier density accompanied with the presence of some trap states[21,34,56] or/and charge separation accumulated a reverse electric field which suppressed further injec-

Fig. 7 (a) Photocurrent (extracted from the V_g value of −40 V) of DTTQ : QD (3 : 7) hybrid phototransistor as a function of illumination light intensity. (b) Dependence of photoresponsivity, photosensitivity, and detectivity on the illumination light intensity. The values were extracted from the V_g values of 60 V, −40 V, and 60 V for the photoresponsivity, photosensitivity, and detectivity, respectively.

tion of electrons from the QDs to the DTTQ layer.[57] The increase in the photocurrent and the high α value implied that more photogenerated electrons were transferred to DTTQ and the loss of the photogenerated carriers through recombination was reduced in the hybrid phototransistor.
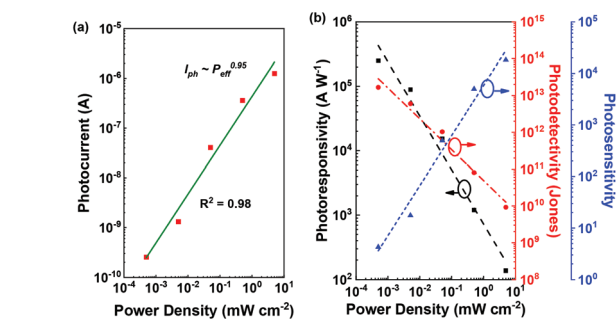
Then, the three performance parameters of photodetection, namely photoresponsivity (R), sensitivity (S), and detectivity (D), of the DTTQ : QD hybrid device were analyzed by the following equations:

$$R = \frac{I_{illum} − I_{dark}}{P_{eff} A} \tag{1}$$

$$S = \frac{I_{illum} − I_{dark}}{I_{dark}} \tag{2}$$

$$D = R\sqrt{\frac{A}{2qI_{dark}}} \tag{3}$$

Here, A and q are the effective channel area and unit charge, respectively. All of these device performance para-

Table 1 Summary of the device performance of hybrid phototransistors based on solution-sheared DTTQ : CsPbBr$_3$ QD thin films under UV light illumination

| DTTQ : QD	R (A W^{-1})	S	D (Jones)
9 : 1	1.1×10^2	14.7	6.3×10^{11}
7 : 3	1.0×10^2	14.9	4.1×10^{11}
5 : 5	1.7×10^3	26.5	1.2×10^{12}
3 : 7	7.1×10^5	1.8×10^4	3.6×10^{13}
1 : 9	2.1×10^5	4.0×10^3	8.1×10^{13}

Fig. 8 (a) Transient photo-switching characteristics and (b) enlarged one-cycle figure of the transient response of the DTTQ : QD (3 : 7) hybrid phototransistor.

meters of the hybrid phototransistors at maximum values are summarized in Table 1. The curves of the calculated R, S, and D values of DTTQ : QD (3 : 7) as functions of the illumination power are shown in Fig. 7(b). Here, R is the indication of how responsive the photodetector was against the incident light. The DTTQ : QD (3 : 7) hybrid phototransistor reached the highest R value of 7.1×10^5 A W^{-1} at P_{eff} of 0.5 μW cm^{-2} among these hybrid devices. The calculated R value exponentially decreased as the incident power increased because of the increased scattering and charge carrier recombination.[58] In addition to R, the D value is an important parameter to evaluate the capability of the phototransistor when detecting weak optical signals. The hybrid device was extremely sensitive to P_{eff}. Both R and D values followed a similar P_{eff} dependent trend, and the D value decreased considerably with increasing P_{eff} value. The resultant D value of the DTTQ : QD (3 : 7) hybrid device was as impressively high as 3.6×10^{13} Jones, particularly when the minimum P_{eff} value was set, which was comparable to the value of the transitional Si-based photodetector.[2] Moreover, the S value was related to the photo-switching ratio calculated from the transfer curves coupled with light illumination, and increased with an increase in the P_{eff} value. The DTTQ : QD (3 : 7) hybrid device presented the maximum S value of 1.8×10^4 under the UV light detection. As the light intensity increased, more charge carriers were generated and transferred to DTTQ, which directly induced the photogating effect and a higher photocurrent as well as a higher S value. The heterojunction phototransistor with DTTQ : QD (3 : 7) was confirmed to yield excellent photo-electrical device performance. The enhancement of light absorption in the spectral range of the 365 nm wavelength with an increase in the perovskite QD stoichiometry was responsible for the improved performance, while still maintaining the efficient charge transport within the organic semiconducting channels.

The dynamic photo-switching characteristics of the hybrid DTTQ : QD heterojunction phototransistor were investigated by periodically pulsed UV light irradiation at 0.5 s intervals at a power density of 5000 μW cm^{-2} and fixed $V_d = 60$ V and $V_g = -40$ V, as shown in Fig. 8(a). This device exhibited a stable and constant transient response to achieve the alternating high and low photocurrent states under the periodic ON/OFF light irradiation. Note that the persistent high photocurrent was still maintained right after removing the illumination (Fig. 6(c)) except when a positive pulse gate bias (50 V for 1 s) was applied to the n-type hybrid transistor.[59,60] The I_d value
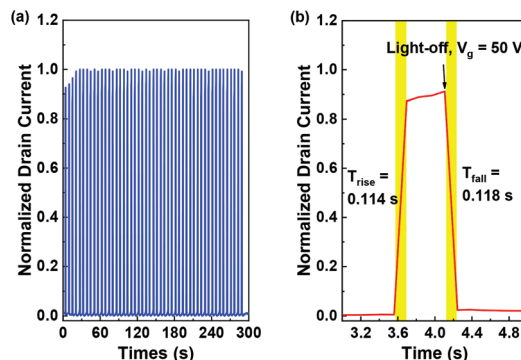
quickly increased when the light was turned on, while it quickly reduced to the dark-state level once the light was switched off with the external voltage bias. This indicated the increased charge carriers' lower energy barrier upon illumination, which allowed the charge tunneling and transport in the dark. Moreover, the photogenerated holes trapped in the QDs led to the photogating effect.[22,61] Removing the light was not sufficient to deplete the accumulation, and the hybrid channel was emptied with holes when the positive pulse bias was applied. In this case, the carrier recombination occurred, and thus I_d returned to the dark-state level (Fig. 6(d)). The rising and falling times were defined as the interval time when the I_d value reached 0%–90% and 90%–10% of the current step height between the turn ON and OFF states, respectively, as shown in Fig. 8(b). The repeatable ON/OFF properties and the concurrently obtained short response time (rising time: 114 ms per falling time: 118 ms) make the hybrid phototransistor a potential candidate for multifunctional photoelectric applications. It is noted here that the real photoresponse time should be faster than the reported ~100 ms since the light source is not synchronized with pulse function generation powered by an electric field (see the input light conditions in Fig. S13†). The long-term stability of the DTTQ : QD (3 : 7) device was also tested. We found that the I_{illum} and I_{dark} values could be still maintained even after 15 days stored in ambient air (Fig. S14†). In addition, the bandgap tunability of perovskite QDs from the UV to the visible and infrared regions will be appreciated as a means to extend the range of the photodetector in organic semiconductor charge-transporting matrices.

4. Conclusions

In summary, we reported the fabrication of solution-processed hybrid small molecule semiconductor:perovskite QD films, which could be used in sensitized phototransistor applications. The spray-assisted LARP method for the preparation of CsPbBr$_3$ QDs with a strong UV light-harvesting ability absorbed photons and delivered the charge carriers to the crys-

talline DTTQ semiconductor component through the built-in field within the bulk heterojunction between the light absorption part and the transport channel. Owing to the excellent *n*-type charge transport properties of DTTQ combined with $CsPbBr_3$ QDs as a photosensitizer, the hybrid phototransistor with a tunable hybrid composition led to the pronounced photoresponse with a remarkable photogating effect under UV light illumination (365 nm wavelength). With the use of the champion DTTQ : QD (3 : 7) photoactive channel, high photodetection performance in terms of $R = 7.1 \times 10^5$ A W^{-1}, $S = 1.8 \times 10^4$, and $D = 3.6 \times 10^{13}$ Jones could be delivered. The solution-processed sensitized hybrid phototransistor proposed here may provide an outstanding direction for developing light-stimulated photodetectors with continuing advances in future materials-device performance optimization.

Conflicts of interest

There are no conflicts to declare.

Acknowledgements

Notes and references

1 H.-P. Wang, S. Li, X. Liu, Z. Shi, X. Fang and J.-H. He, *Adv. Mater.*, 2021, **33**, 2003309.

2 D. Kufer and G. Konstantatos, *ACS Photonics*, 2016, **3**, 2197–2210.

3 Y. Wang, L. Song, Y. Chen and W. Huang, *ACS Photonics*, 2020, **7**, 10–28.

4 Y. Xu and Q. Lin, *Appl. Phys. Rev.*, 2020, **7**, 011315.

5 C. Xie, C.-K. Liu, H.-L. Loi and F. Yan, *Adv. Funct. Mater.*, 2020, **30**, 1903907.

6 F. Pelayo García de Arquer, A. Armin, P. Meredith and E. H. Sargent, *Nat. Rev. Mater.*, 2017, **2**, 16100.

7 N. J. Huo and G. Konstantatos, *Adv. Mater.*, 2018, **30**, 1801164.

8 H. Gu, S. C. Chen and Q. D. Zheng, *Adv. Opt. Mater.*, 2021, **9**, 2001637.

9 J. A. Huang and L. B. Luo, *Adv. Opt. Mater.*, 2018, **6**, 1701282.

10 J. C. Zhou and J. Huang, *Adv. Sci.*, 2018, **5**, 1700256.

11 K. M. Xu, W. J. Zhou and Z. J. Ning, *Small*, 2020, **16**, 2003397.

12 X. H. Liu, D. J. Yu, X. F. Song and H. B. Zeng, *Small*, 2018, **14**, 1801460.

13 Y. X. Wang, G. L. Ding, J. Y. Mao, Y. Zhou and S. T. Han, *Sci. Technol. Adv. Mater.*, 2020, **21**, 278–302.

14 H. Wang and D. H. Kim, *Chem. Soc. Rev.*, 2017, **46**, 5204–5236.

15 M. Ahmadi, T. Wu and B. Hu, *Adv. Mater.*, 2017, **29**, 1605242.

16 C. Li, W. Huang, L. Gao, H. Wang, L. Hu, T. Chen and H. Zhang, *Nanoscale*, 2020, **12**, 2201–2227.

17 Y. Wang, Y. Liu, S. Cao and J. Wang, *J. Mater. Chem. C*, 2021, **9**, 5302–5322.

18 Y. Wei, Z. Y. Cheng and J. Lin, *Chem. Soc. Rev.*, 2019, **48**, 310–350.

19 X. Gong, M. Tong, Y. Xia, W. Cai, J. S. Moon, Y. Cao, G. Yu, C.-L. Shieh, B. Nilsson and A. J. Heeger, *Science*, 2009, **325**, 1665–1667.

20 C. Tyznik, J. Lee, J. Sorli, X. Liu, E. K. Holland, C. S. Day, J. E. Anthony, Y.-L. Loo, Z. V. Vardeny and O. D. Jurchescu, *ACS Appl. Mater. Interfaces*, 2021, **13**, 10231–10238.

21 H. Wu, Z. Kang, Z. Zhang, H. Si, S. Zhang, Z. Zhang, Q. Liao and Y. Zhang, *Small Methods*, 2019, **3**, 1900117.

22 C. Jo, S. Lee, J. Kim, J. S. Heo, D.-W. Kang and S. K. Park, *ACS Appl. Mater. Interfaces*, 2020, **12**, 58038–58048.

23 H. Wu, H. Si, Z. Zhang, Z. Kang, P. Wu, L. Zhou, S. Zhang, Z. Zhang, Q. Liao and Y. Zhang, *Adv. Sci.*, 2018, **5**, 1801219.

24 Y. Hou, L. Wang, X. Zou, D. Wan, C. Liu, G. Li, X. Liu, Y. Liu, C. Jiang, J. C. Ho and L. Liao, *Small*, 2020, **16**, 1905609.

25 Y. Yu, Y. Zhang, Z. Zhang, H. Zhang, X. Song, M. Cao, Y. Che, H. Dai, J. Yang, J. Wang, H. Zhang and J. Yao, *J. Phys. Chem. Lett.*, 2017, **8**, 445–451.

26 J. Jiang, X. Zou, Y. Lv, Y. Liu, W. Xu, Q. Tao, Y. Chai and L. Liao, *Nat. Commun.*, 2020, **11**, 4266.

27 Z.-Y. Peng, J.-L. Xu, J.-Y. Zhang, X. Gao and S.-D. Wang, *Adv. Mater. Interfaces*, 2018, **5**, 1800505.

28 X. Liu, W. Kuang, H. Ni, Z. Tao, Q. Huang, J. Chen, Q. Liu, J. Chang and W. Lei, *Nanoscale*, 2018, **10**, 10182–10189.

29 L. Qian, Y. Sun, M. Wu, D. Xie, L. Ding and G. Shi, *Adv. Mater.*, 2017, **29**, 1606175.

30 A. Surendran, X. Yu, R. Begum, Y. Tao, Q. J. Wang and W. L. Leong, *ACS Appl. Mater. Interfaces*, 2019, **11**, 27064–27072.

31 C. Xie, P. You, Z. Liu, L. Li and F. Yan, *Light: Sci. Appl.*, 2017, **6**, e17023–e17023.

32 C. Zou, Y. Xi, C.-Y. Huang, E. G. Keeler, T. Feng, S. Zhu, L. D. Pozzo and L. Y. Lin, *Adv. Opt. Mater.*, 2018, **6**, 1800324.

33 K. Wang, S. Dai, Y. Zhao, Y. Wang, C. Liu and J. Huang, *Small*, 2019, **15**, 1900010.

34 X. Xu, W. Deng, X. Zhang, L. Huang, W. Wang, R. Jia, D. Wu, X. Zhang, J. Jie and S.-T. Lee, *ACS Nano*, 2019, **13**, 5910–5919.

35 Y. Chen, Y. Chu, X. Wu, W. Ou-Yang and J. Huang, *Adv. Mater.*, 2017, **29**, 1704062.

36 S. H. Yu, Y. Lee, S. K. Jang, J. Kang, J. Jeon, C. Lee, J. Y. Lee, H. Kim, E. Hwang, S. Lee and J. H. Cho, *ACS Nano*, 2014, **8**, 8285–8291.

37 Y. Huang, F. Zhuge, J. Hou, L. Lv, P. Luo, N. Zhou, L. Gan and T. Zhai, *ACS Nano*, 2018, **12**, 4062–4073.

38 G. Yu, J. Gao, J. C. Hummelen, F. Wudl and A. J. Heeger, *Science*, 1995, **270**, 1789.

39 Y.-J. Cheng, S.-H. Yang and C.-S. Hsu, *Chem. Rev.*, 2009, **109**, 5868–5923.

40 A. Facchetti, *Chem. Mater.*, 2011, **23**, 733–758.

41 B. Qiu, Z. Chen, S. Qin, J. Yao, W. Huang, L. Meng, H. Zhu, Y. Yang, Z.-G. Zhang and Y. Li, *Adv. Mater.*, 2020, **32**, 1908373.

42 Y. J. Su, S. C. Huang, T. W. Chen, L. C. Chueh, Y. Cui, L. Hong, H. F. Yao, J. H. Hou, J. T. Chen and C. S. Hsu, *ACS Appl. Mater. Interfaces*, 2021, **13**, 26247–26255.

43 T. Chiba, K. Hoshi, Y.-J. Pu, Y. Takeda, Y. Hayashi, S. Ohisa, S. Kawata and J. Kido, *ACS Appl. Mater. Interfaces*, 2017, **9**, 18054–18060.

44 S. Vegiraju, G.-Y. He, C. Kim, P. Priyanka, Y.-J. Chiu, C.-W. Liu, C.-Y. Huang, J.-S. Ni, Y.-W. Wu, Z. Chen, G.-H. Lee, S.-H. Tung, C.-L. Liu, M.-C. Chen and A. Facchetti, *Adv. Funct. Mater.*, 2017, **27**, 1606761.

45 Y. Wang, L. Varadi, A. Trinchi, J. Shen, Y. Zhu, G. Wei and C. Li, *Small*, 2018, **14**, 1803156.

46 S.-W. Dai, B.-W. Hsu, C.-Y. Chen, C.-A. Lee, H.-Y. Liu, H.-F. Wang, Y.-C. Huang, T.-L. Wu, A. Manikandan, R.-M. Ho, C.-S. Tsao, C.-H. Cheng, Y.-L. Chueh and H.-W. Lin, *Adv. Mater.*, 2018, **30**, 1705532.

47 B. A. Koscher, J. K. Swabeck, N. D. Bronstein and A. P. Alivisatos, *J. Am. Chem. Soc.*, 2017, **139**, 6566–6569.

48 T. Chiba, Y. Hayashi, H. Ebe, K. Hoshi, J. Sato, S. Sato, Y.-J. Pu, S. Ohisa and J. Kido, *Nat. Photonics*, 2018, **12**, 681–687.

49 Y. Lee, J. Kwon, E. Hwang, C.-H. Ra, W. J. Yoo, J.-H. Ahn, J. H. Park and J. H. Cho, *Adv. Mater.*, 2015, **27**, 41–46.

50 H. Liu, X. Zhang, L. Zhang, Z. Yin, D. Wang, J. Meng, Q. Jiang, Y. Wang and J. You, *J. Mater. Chem. C*, 2017, **5**, 6115–6122.

51 K.-J. Baeg, M. Binda, D. Natali, M. Caironi and Y.-Y. Noh, *Adv. Mater.*, 2013, **25**, 4267–4295.

52 E. Baek, T. Rim, J. Schutt, C. K. Baek, K. Kim, L. Baraban and G. Cuniberti, *Nano Lett.*, 2017, **17**, 6727–6734.

53 Y. Zou, F. Li, C. Zhao, J. Xing, Z. Yu, W. Yu and C. Guo, *Adv. Opt. Mater.*, 2019, **7**, 1900676.

54 R. Begum, M. R. Parida, A. L. Abdelhady, B. Murali, N. M. Alyami, G. H. Ahmed, M. N. Hedhili, O. M. Bakr and O. F. Mohammed, *J. Am. Chem. Soc.*, 2017, **139**, 731–737.

55 Z. Li, J. Li, D. Ding, H. Yao, L. Liu, X. Gong, B. Tian, H. Li, C. Su and Y. Shi, *ACS Appl. Mater. Interfaces*, 2018, **10**, 36493–36504.

56 S. Pak, Y. Cho, J. Hong, J. Lee, S. Lee, B. Hou, G.-H. An, Y.-W. Lee, J. E. Jang, H. Im, S. M. Morris, J. I. Sohn, S. Cha and J. M. Kim, *ACS Appl. Mater. Interfaces*, 2018, **10**, 38264–38271.

57 L.-B. Luo, G.-A. Wu, Y. Gao, L. Liang, C. Xie, Z.-X. Zhang, X.-W. Tong, T. Wang and F.-X. Liang, *Adv. Opt. Mater.*, 2019, **7**, 1900272.

58 D. Kufer, I. Nikitskiy, T. Lasanta, G. Navickaite, F. H. L. Koppens and G. Konstantatos, *Adv. Mater.*, 2015, **27**, 176–180.

59 R. Jia, X. Wu, W. Deng, X. Zhang, L. Huang, K. Niu, L. Chi and J. Jie, *Adv. Funct. Mater.*, 2019, **29**, 1905657.

60 H. Zhu, A. Liu, H. Kim, J. Hong, J.-Y. Go and Y.-Y. Noh, *Chem. Mater.*, 2021, **33**, 1174–1181.

61 G. Konstantatos, M. Badioli, L. Gaudreau, J. Osmond, M. Bernechea, F. P. G. de Arquer, F. Gatti and F. H. L. Koppens, *Nat. Nanotechnol.*, 2012, **7**, 363–368.